3D phase contrast MRI in models of human airways - validation of computational fluid dynamics simulations of steady inspiratory flow

Abstract:

Background: Knowledge of airflow patterns in the large airways is of interest in obstructive airways disease and in the development of inhaled therapies. Computational Fluids Dynamics (CFD) simulations are used to study airflow in realistic airway models but usually need experimental validation.

Purpose: To develop MRI based methods to study airway flow in realistic 3D printed models.

Study type: case control.

Phantom: two 3D printed lung models.

Field strength/sequence: 1.5 & 3T, flow MRI

Assessment: Two human airway models, respectively including and excluding the oral cavity and upper airways derived from MR and CT imaging, were 3D printed. 3D flow MRI was performed at different flow conditions corresponding to slow and steady airflow inhalation rates. Water was used as the working fluid to mimic airflow. Dynamic acquisition of 1D velocity profiles was also performed at different locations in the trachea to observe variability during non-steady conditions.

Statistical tests: Linear regression analysis to compare both flow velocity fields and local flow rates from CFD simulations and experimental measurement with flow MRI.

Results: A good agreement was obtained between 3D velocity maps measured with flow MRI and predicted by computational fluid dynamics simulations, with linear regression R-squared values ranging from 0.39 to 0.94 when performing a pixel by pixel comparison of each velocity component. The flow distribution inside the lung models was also similar with average slope and R-squared values of 0.96 and 0.99 respectively when comparing local flow rates assessed at different branching locations of the models. In the model that included the upper airways, a turbulent laryngeal jet flow was observed with both methods and affected remarkably the velocity profiles in the trachea.

Data conclusion: We propose flow MRI using water as a surrogate fluid to air, as a validation tool for computational fluid dynamics simulations of airflow in geometrically realistic models of the human airways.

Key Words: airflow, lungs, CFD, 3D printing model

INTRODUCTION

Knowledge of airflow patterns in the airways is of medical interest in obstructive airways diseases and in the development of inhalation therapies. Computational modeling has provided important information for optimizing methods of inhaled drug delivery [1-4] and understanding risks posed to the lungs by air pollutants [5]. Early studies of airway flow were based on idealized airways and simplistic models of lung diseases [1, 3]. With computational advances and improved anatomical imaging, computational fluid dynamics (CFD) simulations are now well established in the study of flow patterns in anatomically accurate airway geometries [6, 7]. With CFD simulations it has been demonstrated, that realistic (and subject specific) airways anatomy plays a major role in the determining flow and particle distribution [8, 9]. Nevertheless, CFD simulations require validation.

Experimentally, flow can be measured in vitro with hot wire anemometry [10] or laser based methods such as laser Doppler anemometry [11], Doppler particle analysis [12] and particle image velocimetry [13, 14]. Recent advances in 3D printing have helped in the development of these methods but laser techniques are inherently constrained by optical access of the 3D model and the requirement to seed the fluid with tracer particles. Whereas hot wire anemometry measurements are not reliable in zones with recirculation and secondary flows.

Phase contrast velocimetry (PCV-MRI) is a non-invasive technique capable of measuring the velocity vector of any MR sensitive fluid in motion inside complex 3D geometries [15]. It can be used in vivo or in vitro to measure laminar and turbulent, single and multiphase flows where other measurement modalities are not applicable. PCV-MRI has been proposed for validation of CFD simulations of blood flow in 3D printed patient specific models of cerebral aneurysm [16], coronary aneurysm [17], the aorta [18] and for quantitatively comparing in vivo blood velocity

maps in the vascular system with CFD simulations [19-21]. PCV-MRI has also been applied to gas flow with the measurement in vivo of velocity maps in the large airways with hyperpolarized ^{3}He [22-25] and ^{129}Xe [26] and in vitro in 3D printed models of pulmonary airways for CFD validation [27, 28]. However, hyperpolarized gases are expensive and measuring the gas signal involves additional challenges due to dephasing by diffusion in the presence of magnetic field gradients and due to the non-renewable polarization. Alternatively, SF_6 gas MRI has been proposed for PCV-MRI measurement of turbulent gas flow in vitro [29] but this thermally polarized gas has a much weaker MR signal still making high resolution PCV mapping of flow technically challenging.

Since single-phase flow inside a rigid model can be fully characterized by its Reynolds and Womersley numbers, another possibility is to use a liquid as a surrogate fluid to mimic gas flow inside 3D printed models of the airways. This principle is routinely implemented in particle image velocimetry experiments, usually with a water-glycerol mixture. In the case of PCV-MRI, doped water has the advantage of being a natural, cheap and abundant source of proton spin signal for which PCV-MRI sequences are generally available on MR scanners nowadays. Jalal et al. [30] applied this surrogate method in an idealized model of a symmetric planar double airway bifurcation under steady flow covering a range of flow regimes (from laminar to turbulent flows). Similar experiments were performed by Banko et al. [31], in a realistic 3D printed model of the human airways during constant inspiratory flow rate of 60 L/min corresponding to a peak inflow during moderate exertion. The influence of the extra thoracic airways included in their model, was found to have a significant impact on the flow structures in the trachea and the first bifurcations. This study was performed outside the laminar regime (Reynolds number ~ 4213 in the trachea) but turbulences were not directly observed since the mean velocity field was measured over a long

acquisition time of 90 min. It was assumed that the differences between average flow fields in steady and unsteady conditions are negligible. More recently, the experimental results were compared to CFD simulations performed with the same geometry as the model showing good agreement [32]. The same group extended experimental flow measurement to 4D PCV-MRI with 3D measurement of the 3 velocity components in the same airway model during oscillatory flow [33].

In this work, we aim to demonstrate that MR imaging based methods can be used as an investigative tool to study airflow pattern in vitro and as a validation tool for CFD simulation. We made the following hypotheses: it is possible to combine imaging methods to produce subject specific and realistic 3D printed models of human airways, 3D PCV-MRI measurements using water in vitro to mimic steady laminar airflow during inhalation will show a close resemblance to CFD simulations performed in the same models, the extra thoracic airways have a remarkable effect on the airflow pattern in the major airways, and it is possible to use PCV-MRI measurement to observe turbulent flow.

METHODS

Airway models and experimental flow setup

Two airway models were used for the study. The first model (see Fig. 1.a) consists of a subject specific central airway tree (from the trachea to fifth / sixth generation) derived from the high resolution CT scan from a healthy subject (female, 20 years-old) acquired at total lung capacity. This model was 3D printed on a laser-sintering machine at the scale of 1.5:1 [34]. The second model (see Fig. 1.b) combines the geometry from two sets of scans : (i) the central airways (from trachea to the fifth / seventh generation) derived from a low dose CT scan acquired at total lung

capacity and (ii) the upper airways and oral cavity derived from a head and neck MRI scan of the same asthmatic subject (female, 49 years-old, five pack-year smoking history and limited lung capacity: FEV_1 predicted = 70 %, FEV_1/FVC = 64 % and Global Initiative for Asthma classification = 4). The Institutional Review Board approved use of imaging data with a waiver of informed consent.

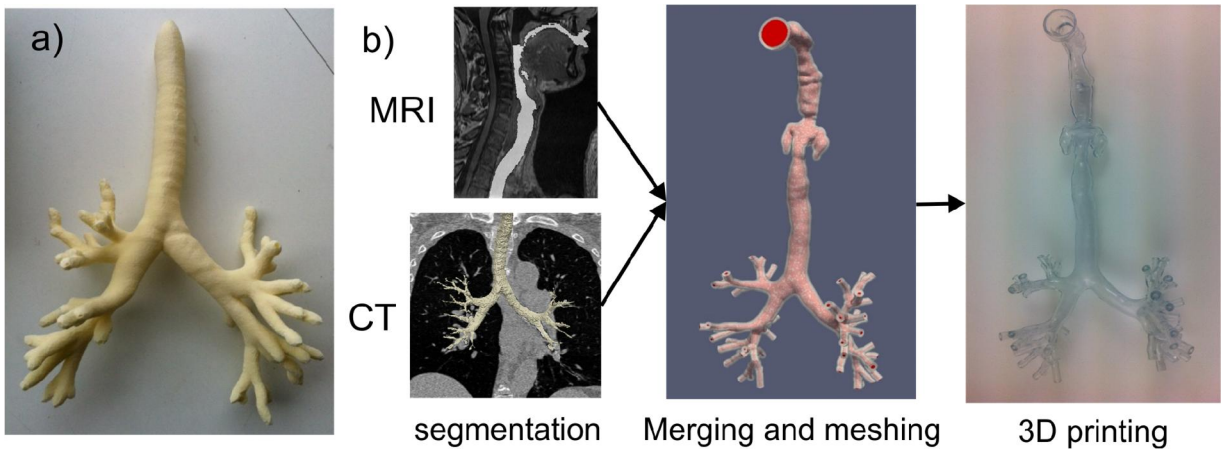

Figure 1: 3D printed models of the two patient-specific lung central airways used for the study. **a)**: first model, central airways only, **b)**: workflow for the creation of the second model including the upper airways and oral cavity derived from the segmentation of MRI images.

The MRI sequence parameters for the proton scan of the upper airways were the following: 1.5 T scanner (GE, HDx, USA) with a head and neck coil during free breathing, 3D fast spoiled gradient echo sequence, 0.5x0.5x1 mm^3 resolution, echo time (T_E) of 5 ms and repetition time (T_R) of 11.5 ms, 12° flip angle (FA), bandwidth of 31.2 kHz and acquisition time of 4.5 min. The CT images were segmented using Mimics (Materialise, Leuven, Belgium) and the head and neck MRI was segmented using ScanIP (Simpleware, Exeter, UK). The CT and MRI segmented models were then merged, meshed and 3D printed by Materialise (Leuven, Belgium) using stereolithography (TuskXC2700T / Tusk2700W material, Tusk, Somos®, Elgin, IL) at the scale of 1:1.

The airways models were supported on a custom holder and immersed in a container placed at the isocentre of the MRI scanner and filled with water doped with copper sulphate at the concentration of 15 mmol/L. The inlet section (the trachea or the oral cavity) was connected to a water reservoir via a long circular pipe of 2 cm diameter in order to obtain a fully developed flow. The flow rate was controlled with a valve at the output of the container and held constant by keeping the same head of water in the reservoir.

A single-phase steady flow inside a rigid model can be fully characterized by its Reynolds number:

$$Re = \frac{\rho Q D_H}{\mu A} \quad [1]$$

where ρ is the density, Q is the volumetric flow rate, μ is the dynamic viscosity ($8.89\ 10^{-4}$ Pa.s), A is the cross sectional area and D_H is the hydraulic diameter (2 and 1.4 cm for the model without and with the upper airways respectively). Therefore, it is possible to use water to mimic airflow inside the lung models, as originally proposed in [35] and recently published in [31]. The model with central airways only was scanned with a 3D PCV-MRI sequence at two different water flow rates of 3.7 and 8 mL/s which are equivalent to low inspiratory airflows of 58 and 125 mL/s respectively. This corresponds to Reynolds numbers in the trachea of 235 and 509 respectively. Since the Reynolds number decreases as airway generation increases with depth into the lungs, it can be assumed that the flow is steady and laminar in the phantom at these flow rates. The same sequence was then used to scan the second model (with upper airways and oral cavity) at a constant flow rate of 3.5 mL/s corresponding to inspiratory airflow of 55 mL/s (Re = 318 in the trachea). However, at the location of the constriction between the tip of the epiglottis and the pharyngeal wall, the airway diameter is reduced to ~5 mm and Re = 890. In order to observe a more physiologically realistic flow regime and the formation of the laryngeal jet flow and its influence

on downstream tracheal flow patterns, the velocity profile was measured with additional 2D/1D PCV-MRI experiments at different axial locations from the larynx to the carina bifurcation. The experimental flow rates were the following: 4.5, 6, 13, 20 and 27 mL/s corresponding to inspiratory airflows (Re in trachea) of 70 (409), 94 (545), 204 (1181), 314 (1816) and 424 mL/s (2452) respectively.

PCV-MRI methods

3D flow PCV-MRI measurements were performed on a 3 T MRI scanner (Philips, Ingenia, Netherlands) with a multi-channel cardiac coil. A 3D fast field echo sequence with flow encoding gradients applied on the 3 axes was used with a partial echo in the frequency direction, a bandwidth per pixel of 190 Hz and a 5° flip angle. Additional imaging parameters were adjusted depending on the velocity encoding (Venc) value chosen for the experiments and the model size and are summarized in table 1. As a result of the broad range of velocities encountered in the model including the upper airways, the acquisition was repeated twice with two different maximum velocity encoding values of 30 and 10 cm/s. The acquision time for the 3D field …

2D/1D velocity profiles measurements were performed on a 1.5 T scanner (GE, HDx, USA) with a birdcage head coil and a 2D Cartesian encoded spoiled gradient echo sequence with the flow encoding gradient perpendicular to the slice orientation and a 2-interleave balanced velocity encoding scheme. The following parameters were used: field of view (FOV) of 250 x 187.5 mm^2, resolution of 0.98 mm and 1.95 mm in the frequency and phase direction respectively, slice thickness of 6 mm, flip angle between 60 to 70°, $7.4 < T_E < 10.7$ ms, $14 < T_R < 17$ ms, $4.7 <$ Venc < 62.7 cm/s and a bandwidth of 31.3 kHz. The acquisition time for each 2D slice was approximately 3 s. Five slices from the trachea entrance to the carina were acquired for each

experimental flow corresponding to a full acquisition time of ~ 15 s. To obtain successive time-resolved 1D velocity profiles, the sequence was repeated with phase encoding gradients off. The time resolution between two successive 1D velocity profiles was therefore 2 x T_R ~ 30 ms.

CFD simulations

The luminal spaces within the segmented geometries of the airway models were filled with unstructured meshes for CFD analysis. The hybrid volume meshes consisted of tetrahedrons and near wall prism layer elements and were created using Ansys ICEM CFD (Ansys, Abingdon, UK). As a consequence, a total of 5.2 million volume meshes in the lower airway only model, and 11.3 million meshes in the combined lower and upper airway model were generated to attain mesh independent solutions and to resolve the small-scale flow structures and activities in the trachea. The meshed model geometries were imported into the finite volume CFD solver, Ansys CFX (Ansys, Abingdon, UK), that was used to solve the unsteady, incompressible Navier-stokes equations. The governing equations were discretised with a second-order accurate central differencing scheme. The pressure and velocity coupling was handled using the PISO algorithm. In this solver, the surfaces of the airways walls were defined as rigid and non-slip to reproduce the boundary conditions in the phantom model. Water was used as the working fluid for the CFD simulations with density and dynamic viscosity values of 997.6 kg/m^3 and 8.89 × 10^{-4} Pa·s, respectively. The experimental water flow rates were used at the inlet boundaries while a traction free boundary condition was applied at the outlets at distal branches (pressure at outlet boundaries uniformly constant = 0 Pa). For flow simulations, we assumed incompressible flow and a Newtonian fluid. The laminar flow condition was used for the experimental lower-flow conditions (water flow rate from 3.5 to 8 mL/s). The flow was computed at every millisecond for 21 seconds and the data in last 3 seconds were averaged and used to compare with the experimental

measurements to avoid an influence of initial conditions. The large eddy simulation (LES) technique was used for the higher-flow condition (20 mL/s). In this model the subgrid-scale stresses were modelled with the wall-adapting local eddy-viscosity (WALE) model [36]. The CFD simulations were carried out on the 396 cores of high-performance computing system at the Warwick Centre for Scientific Computing.

Data Processing

DICOM images from the 3D PCV MRI experiments were imported into ScanIP software (Simpleware, Exeter, UK) for semi-automatic segmentation of the region of interest corresponding to the inner part of the lung airways model. The resulting 3D model was eroded by 1 pixel in order to exclude the boundary layer flow region where partial volume effects might occur and where velocities and therefore velocity-to-noise ratios are low. The three velocity components were extracted from DICOM images using MATLAB (Mathworks, Natick, MA) and exported into Paraview [37] after multiplication by the generated mask. Computational datasets from CFD simulations were also imported into Paraview, registered manually to the experimental dataset and resampled in order to match the resolution of the MRI images. Pixel by pixel comparison of both flow velocity fields was performed for each velocity component in Matlab using linear regression analysis. In addition, the local flow rates at different locations of the models (from trachea to segmental flow rates) were compared between MRI and CFD.

2D/1D velocity profiles were reconstructed directly from the raw data in MATLAB using phase difference reconstruction to extract the transverse component of the velocity for each pixel. The 2D images were compared qualitatively with the average velocity map resulting from the CFD simulations at the same location. They were also used to extract the pixels of interest from the 1D

velocity profiles data that were acquired at the same slice locations in the trachea. The custom 3D printed support for the lung model was designed to cover any space under and above the trachea (phase direction in the 2D images), such that only flowing spins inside the trachea would contribute to the measured 1D velocity profile. Consecutive velocity profiles were plotted and compared with results from the CFD simulations obtained from the corresponding slice locations at the same temporal resolution (~ 30 ms).

RESULTS

The CFD flow simulations demonstrated reasonable agreement with the MRI measurements. Figure 2 presents a qualitative and a quantitative comparison between CFD simulations and PCV-MRI measurements in the lung model of the central airways at the steady flow rate equivalent to an inspiratory airflow of 58 mL/s. A close resemblance between the velocity distributions in the airways of the model can be observed (Fig. 2.a & 2.b). The parabolic inlet velocity profile stays nearly unchanged in the trachea, only shifted towards the left lung due to the trachea's curvature. Higher velocity values are observed in the left main bronchus when compared to the right main bronchus due to a smaller cross sectional area, but comparable flow rates going into each lung are measured (49/51 % ratio for CFD and 56/44 % for MRI). The regression analysis between CFD and MRI measurement of the velocity components is shown in Fig. 2.c, 2.d & 2.e and the results (y-intercept, slope, R^2) are summarized in table 2 together with results obtained at Q = 8 mL/s (equivalent Q_{air} of 125 mL/s). Similar values were obtained for both experimental flow rates. In addition to the velocity comparison, the lobar and segmental flow rates calculated from CFD and MRI measurements are presented in figure 2.f for both flow rate conditions. The MRI flow measurements were found to be consistent with CFD simulation. The regression analysis gave the following results: y-intercept = 0.04±0.03 mL/s, slope = 0.98±0.01, R^2 = 0.99, which confirms that

the flow distribution among the airways is similar although the CFD predicted a lower flow in the left lower lobe (24 % instead of 29 %) and a higher flow in the right lower lobe (28 % instead of 22 %) when compared to the flows measured with PCV-MRI in the same locations.

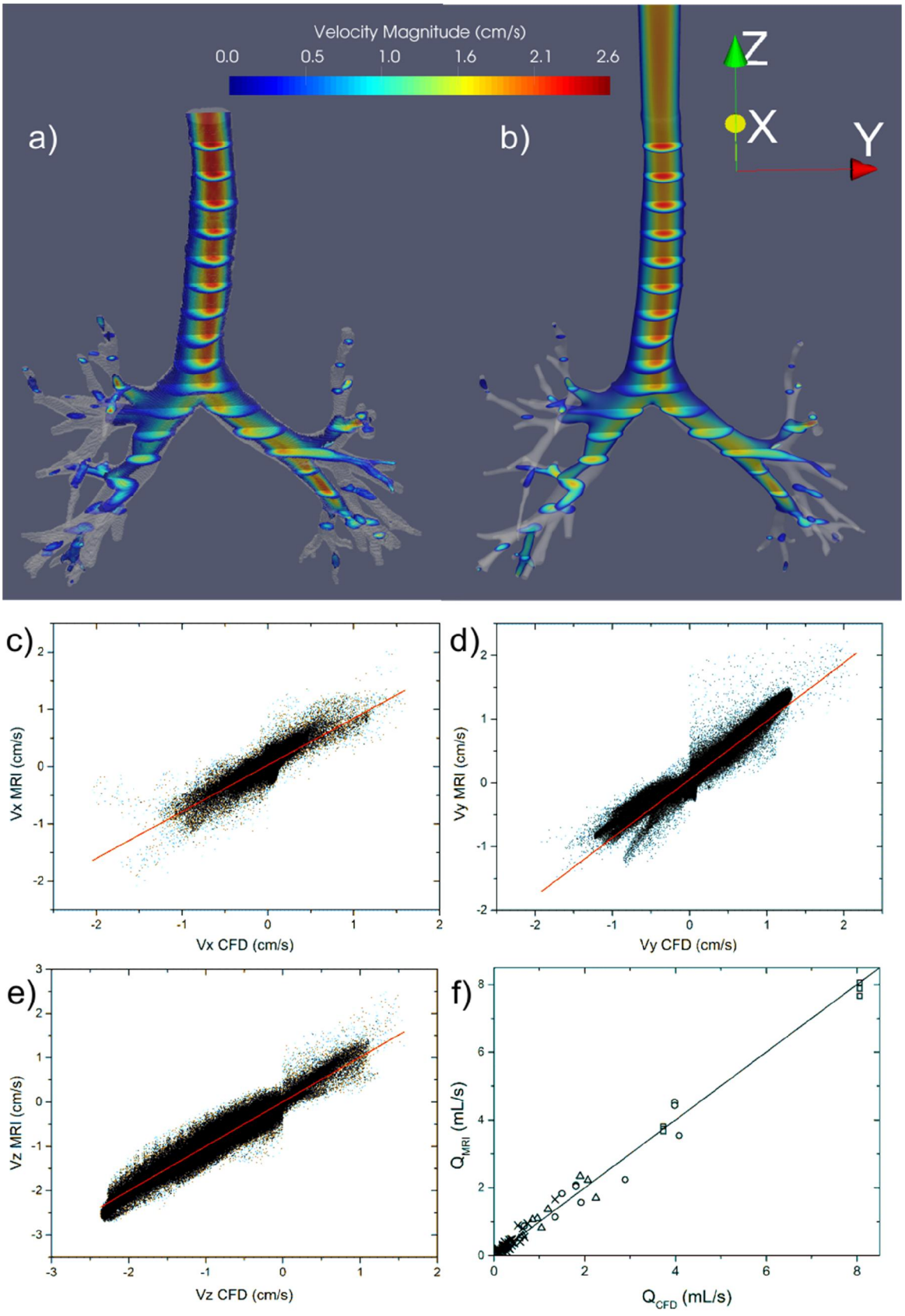
Velocity Magnitude (cm/s)
0.0
0.5
1.0
1.6
2.1
2.6
a)
b)
Z
X
Y
c)
Vx MRI (cm/s)
Vx CFD (cm/s)
d)
Vy MRI (cm/s)
Vy CFD (cm/s)
e)
Vz MRI (cm/s)
Vz CFD (cm/s)
f)
Q_{MRI} (mL/s)
Q_{CFD} (mL/s)

Figure 2 (**USE COLOR**): Comparison between CFD simulations and PCV-MRI measurements in the lung model of the central airways. **a)** & **b)**: 3D visualization of the flow patterns measured by PCV-MRI and predicted by CFD simulations respectively (water flow of 3.7 mL/s). The colormap represents the velocity magnitude in cm/s. **c)**, **d)** & **e)**: pixel by pixel comparison and linear regression line of the velocity values along the x, y and z directions respectively from the data sets displayed in **a)** and **b)** (see axes orientation at the top right corner). **f)**: comparison of the flow values derived from the CFD and MRI data sets at different slice locations (squares: trachea, circles: main bronchi, left lower lobe bronchus and truncus intermedius, triangles: lobes and crosses: segments) for the combined experimental water flows of 3.7 and 8 mL/s (solid line: identity line).

Figure 3 illustrates the results of the comparison between 3D flow PCV-MRI measurements and CFD simulations in the model that included the upper airways and the oral cavity when using a water flow of 3.5 mL/s (equivalent airflow of 55 mL/s). Data from the two different PCV-MRI experiments (different velocity encoding values) were merged and the velocity maps are displayed with a logarithmic scale. Figure 3.a & 3.b show a reasonable agreement with regard to the spatial velocity distributions. When compared with the model with upper airways excluded, the velocity profile is not parabolic in the trachea. The different constrictions and curvatures present in the upper airways and the oral cavity result in a highly asymmetrical flow profile at the entrance of the trachea, biased toward its front wall, which agrees with previous in vivo measurements [26] and CFD simulations [14] that took in to account the effects of the upper airways. The peak velocities are located in the laryngopharynx likely due to the constriction at the epiglottis. Figure 3.c shows a linear regression between the velocity along z (superior to inferior direction) of the MRI voxel datum and corresponding velocities in the CFD model. The regression results (y-intercept, slope, R^2) are presented in table 2. In Fig. 3.d, a comparison of the tracheal, main bronchi and lobar flow rates derived from CFD simulations and experimental measurements is also displayed. The flow distribution inside the model is in good agreement and the following regression analysis results were obtained (0.08±0.05 mL/s, 0.94±0.03, 0.99).

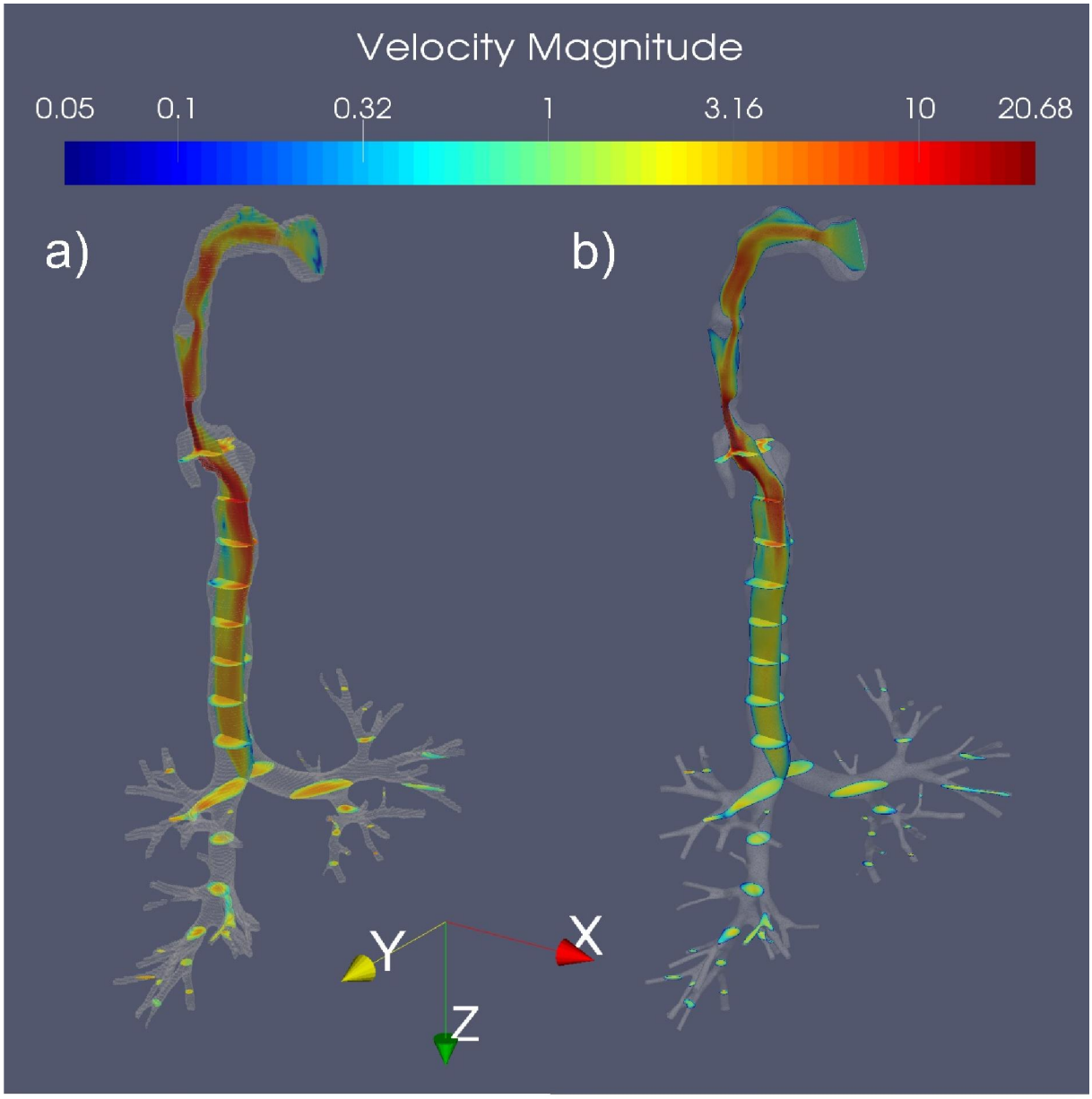
Velocity Magnitude
0.05
0.1
0.32
1
3.16
10
20.68
a)
b)
Y
X
Z

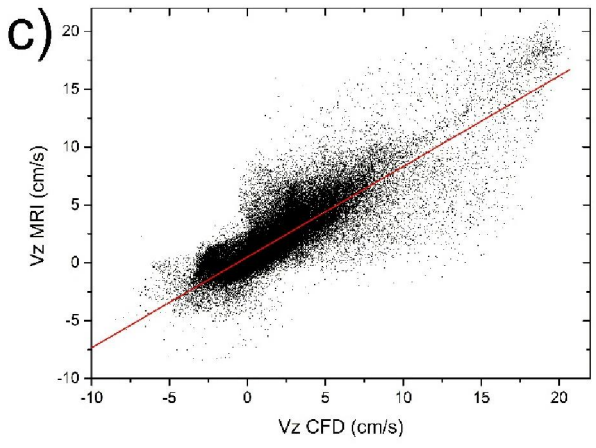
c)
Vz MRI (cm/s)
Vz CFD (cm/s)
20
15
10
5
0
-5
-10
-10
-5
0
5
10
15
20

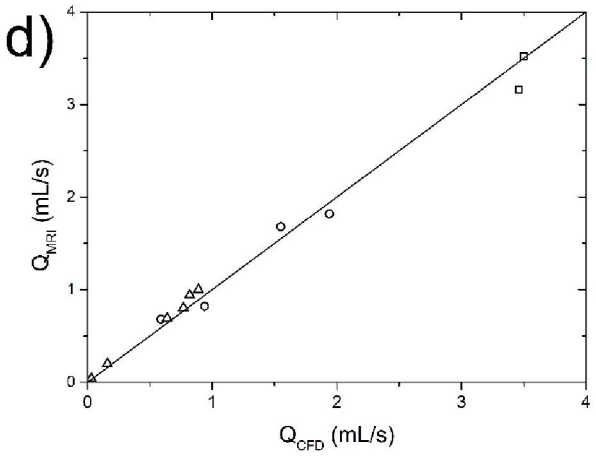
d)
Q_{MRI} (mL/s)
Q_{CFD} (mL/s)
0
1
2
3
4

Figure 3 (**USE COLOR**): Comparison between CFD simulations and PCV-MRI measurements in the lung model of the central and upper airways for a water flow of 3.5 mL/s. **a)** & **b)**: 3D visualization of the flow patterns measured by PCV-MRI and predicted by CFD simulations respectively. The colormap represents the velocity magnitude in cm/s and uses logarithmic scale. **c)**: pixel by pixel comparison and linear regression line of the velocity values along the z direction (see axes orientation at the bottom of **a)**). **d)**: Comparison of the flow values derived from the CFD and MRI data sets at different slice locations (squares: trachea, circles: main bronchi, left lower lobe bronchus and truncus intermedius, triangles: lobes).

In Figure 4, a summary of the comparison between the 2D/1D PCV-MRI measurements and CFD simulations is presented. The velocity maps and profiles of Fig. 4.a to 4.e were obtained at 5 different cross sections (see Fig. 4.f) with an equivalent airflow of 314 mL/s. The successive 1D velocity profiles acquired with a time resolution of 30 ms clearly show flow instability that decreases further down the trachea. This was confirmed by the CFD simulations that predict turbulent jet flow at the beginning of the trachea, which is created by the constriction of the airways by the epiglottis. The standard deviations of the successive velocity profiles were plotted for both CFD and MRI measurements in Fig. 4.g. Although the values seem to be consistently higher for the PCV-MRI measurements (except for the first cross section), the same decreasing trend is seen in the CFD simulations and a reasonable agreement is obtained. The corresponding 2D velocity maps also show good similarities although those were acquired over an acquisition time of 3s that is much longer than the time scale of the turbulence and therefore, results from 2D PCV-MRI measurements need to be interpreted cautiously as a time-averaged representation of flow. However, negative axial velocities are observed in the two first cross sections, which is confirmed by the CFD simulations. This implies that a vortex is present at the entrance of the trachea. In Fig. 4.h, the standard deviation of the velocity profile (normalized by the average velocity) at the cross section S4 for different experimental flows (Q = 4.5, 6, 13, 27 mL/s) is plotted. As expected, a clear increase in instability (turbulence) of the velocity profile is observed as the flow increases.

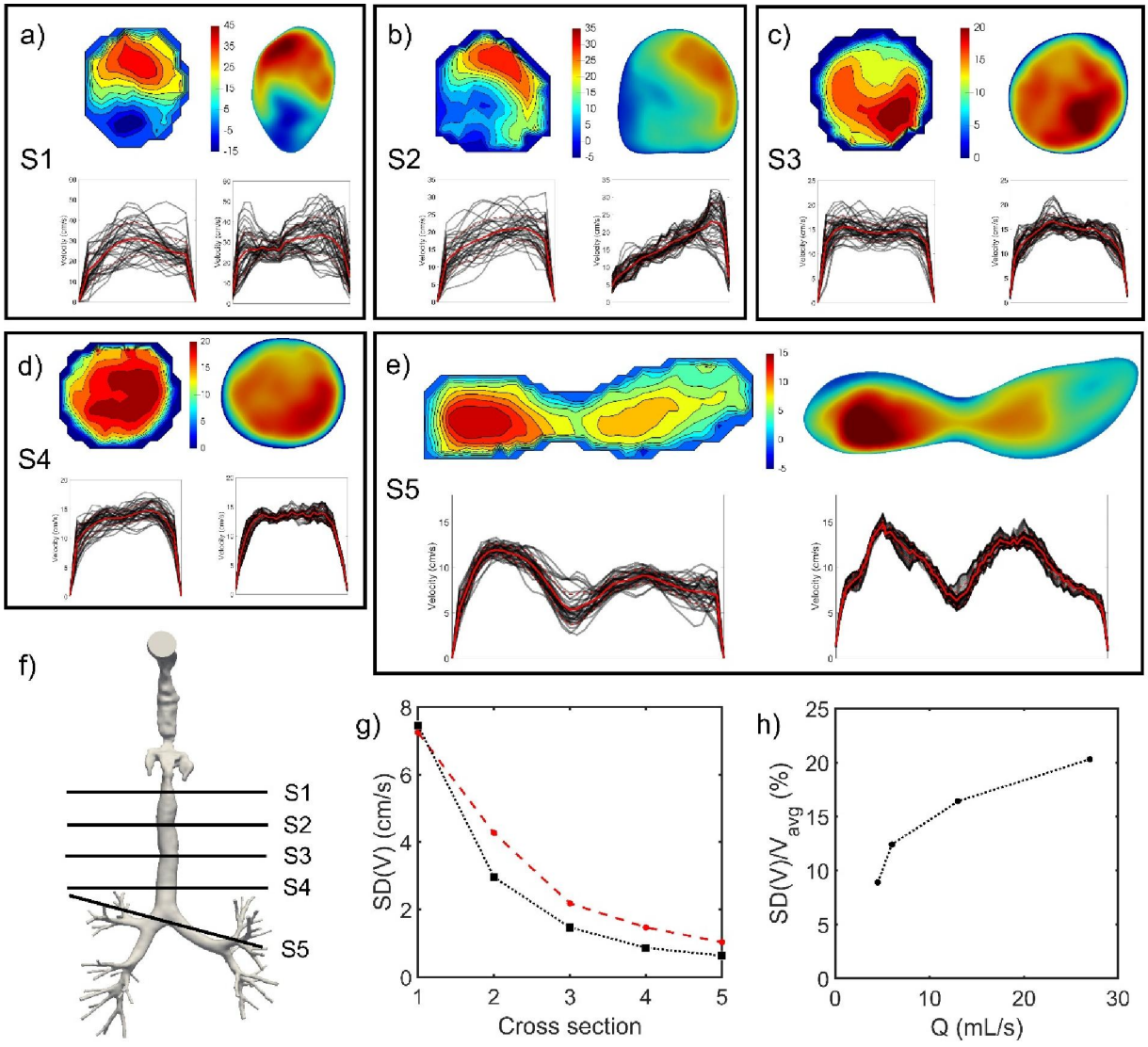

Figure 4 (**USE COLOR**): Comparison between CFD simulations and 2D/1D PCV-MRI measurements in the lung model of the central and upper airways. **f)**: Schematic representation of the positions of the cross sections. **a)** to **e)**: 2D (top)/1D (bottom) velocity profiles comparison between CFD simulations (right) and PCV-MRI measurement (left) for cross sections S1 to S5 respectively at Q = 20 mL/s. The colormaps of the 2D velocity profiles are in cm/s. The semi-transparent black lines of each plot represent the successive velocity profiles (time resolution of 30 ms), the red solid line is the average velocity profile ± SD (red dashed solid lines). **g)**: mean standard deviation of the velocity profiles for the different cross sections S1 to S5 at Q = 20 mL/s (red dashed line: MRI measurement, black dotted line: CFD simulation). **f)**: mean standard deviation of the velocity profile normalized by the average velocity at cross section S4 for different experimental flows (Q = 4.5, 6, 13, 27 mL/s).

DISCUSSION

In this work, we demonstrate the feasibility of using in vitro PCV-MRI as a validation tool for CFD simulations of airflow in geometrically exact and subject specific models of the upper airways. A good agreement between the 3D velocity vector fields measured by 3D PCV-MRI and those predicted by CFD simulations was achieved with R^2 values from pixel by pixel regression analysis between 0.39 to 0.94. A smaller R^2 value was consistently obtained for the model containing the upper airways. We believe that this is mainly due to the smaller size of the model that was 3D printed at true scale and therefore has a higher partial volume effect in the small airways. For this reason, the segmental flow rates could not be calculated and only the tracheal, main bronchi and lobar flow rates were compared. The lowest R^2 values were obtained for the left-right direction in the airway model including the upper airways and the anterior-posterior direction for the model without the upper airways. This corresponds in both cases to the direction where the range of velocity was the lowest (the model including the upper airways has a high velocity component in the anterior-posterior direction due to curvature and constriction of the upper airways). The same Venc was used in the three encoding directions and the value was chosen to cover the highest experimental velocity possible in order to avoid wrapping. Because of the anisotropy of the flow, Venc was therefore not optimum for every direction, which resulted in lower velocity to noise ratio and higher uncertainty in the data.

Residual differences between the CFD simulations and PCV-MRI measurements can be explained by slight disagreements with the modeling conditions. The same constant pressure was applied at every outlet of the model as a boundary condition of the CFD simulations and slight differences of pressure head due to differences in the height of each outlet were not taken into account.

In this work water was used as a surrogate fluid to mimic airflow in the airway models. Although the feasibility to perform in vivo experiments with hyperpolarized gas PCV-MRI have been

demonstrated [22, 25, 26], adapting these methods to the level of detail of study of flow needed here would require large quantities of inhaled hyperpolarized gases delivered over several breaths. Moreover, the in vitro flow experiments described in the present study have the advantage over in vivo measurements that no artifacts due to subject motion is present and that experiments can be repeated multiple times with the same controlled flow conditions for sequence optimization. De Rochefort et al. [27] previously validated CFD simulations of airflow in a 3D printed model of the lung with PCV-MRI measurements of hyperpolarized ^{3}He. However, the model did not contain the extra thoracic airways and it was limited to a few 2D cross sections. Water is therefore a much more practical choice for PCV validation of CFD based on reasons of SNR, cost, preexisting MRI sequences and availability of MR hardware, and has enabled higher resolution images (1x1x2 mm^3) of flow patterns when compared to those achieved with gas phase flow MRI measurements previously. However, gases have significantly different fluid dynamic behavior when compared to liquids. The diffusion properties are crucial when considering airflow and gas mixing. Minard et al. [24, 25] demonstrated the importance of the consideration of diffusional gas mixing between streamlines and computed the apparent ^{3}He gas flow in rat pulmonary airways. Although the effect of laminar blurring due to rapid gas diffusion across neighboring flow streams is expected to be less pronounced in human airways than in rats due to the different fluid regimes, apparent gas transport is not negligible at the human scale. Nonetheless, this is less of a concern when studying medium and large size particle deposition for which Brownian force is negligible and effect of gas diffusivity on particle transport can be neglected [38].

Our study also reveals the importance of the upper airways on the tracheal airflow pattern and flow distribution in the subsequent airways. Our results confirm previous CFD simulations performed by Lin et al. [39] who studied the characteristics of the turbulent laryngeal jet and its effect on

airflow in the human intra-thoracic airways. A high-speed laryngeal jet is formed as the flow passes through the glottis and this jet induces turbulent flow in the trachea that significantly affects airway flow pattern. In a comprehensive review of gas flow in the airways by Tawhai et al. [8], the authors stressed the importance of including the upper airways in computational models of airway flow as it is often neglected due to the complexity of the geometry in this region of the airway tract, that complicates its experimental and numerical study. It was also concluded that "The laryngeal jet is the most prominent inhalation flow phenomenon that determines mean and fluctuating behaviors of the flow, downstream of the upper airway in the tracheobronchial airways". Moreover, it is worth noting that Lin et al. [39] also predicted a vortical flow at the entrance of the trachea and that they report different parameters to describe turbulences, such as turbulent kinetic energy and turbulence frequencies using the proper orthogonal decomposition technique. Interestingly, the time history of the velocity at a single point in the vicinity of the centerline of the trachea is also reported for 2 different cases including and excluding the upper airways. In the current work, we present an experimental technique to validate such models by rapid measurement of successive velocity profiles with 1D PCV-MRI. This goes beyond the method employed by Banko et al. [31] that assumed that the measured 3D velocity map of a turbulent flow acquired over several seconds (minutes) is equal to the average velocity map during this period. The potential of 1D PCV-MRI was demonstrated with a reasonable agreement obtained between CFD simulations and PCV-MRI measurements. Differences in standard deviation of velocity profiles can be explained by differences of locations of the cross sections between the scanner experimental planning and manual positioning in the CFD model. It can also be attributed to differences in spatial and time resolution that was higher during CFD simulations. However, CFD data were retrospectively averaged to reproduce the experimental parameters. Lastly, it can be mentioned that this technique

could be useful when studying cyclic airway flows conditions or steady expiratory flows as it was found that mixing of streams from daughter branches is a source of turbulence for expiratory flows as well [12].

Finally, we would like to acknowledge some limitations of our study regarding the translation of the physiological results reported. Over–interpretation of the differences of flow patterns between the airway model of the asthmatic subject and the healthy subject should be avoided. The purpose of the present work was to present a method to validate CFD simulations of airways flow experimentally and not to study the effect of airway disease in asthma on airway flow. A higher number of cases of patient specific 3D models would need to be studied and none of the models used for the study correspond to an average representative model of the upper airways nor the central airways. A model with rigid walls is also not fully representative of the upper airways and in future work a compliant walled phantom could be used. Regarding the CFD simulations, different techniques could have been used. The LES technique was used for the higher-flow condition only whereas the governing Navier-Stokes equations were directly solved without turbulent flow assumptions for the other experimental conditions. This approach required extremely fine meshes that might cause question regarding the reliability of the model. That is why the LES turbulent flow modelling was also alternatively performed on one experimental condition to check that only minor differences were obtained.

In conclusion, ^{1}H MRI sequences have been used to obtain an anatomical 3D model of the upper airways and the oral cavity. MRI segmentation of the upper airways has the advantage of avoiding exposure of the head and neck to ionizing radiation from CT. The possibility of combining two imaging modalities (MRI and CT scans) to 3D print a human airway model from the opening of the mouth down to the 7th airway generation has been demonstrated. In vitro PCV-MRI

measurement has been tested as a validation tool for CFD simulations of airflow in image based models of the airways of a healthy subject and a patient with asthma, respectively excluding and including the upper airways. Water was used as an MR sensitive surrogate for airflow in the experiments by carefully matching the Reynolds number to the desired flow regime. A good overall agreement between in vitro 3D PCV-MRI measurement and CFD simulation was obtained, which validates the use of CFD models for flows in the human airways, provided that appropriate boundary conditions and meshing parameters are used. The extra-thoracic airways were found to be responsible for a turbulent jet flow that has significant impact on the downstream flow structures in the trachea. This was both predicted by CFD simulations and experimentally observed by rapidly measuring successive 1D velocity profiles with by PCV-MRI at different experimental flow regimes and cross sections in the trachea. Further work will focus on developing more realistic models including: compliant materials, more airway generations, different outlet conditions taking into account airway resistance, reproducing in vitro the respiratory flow cycle and measuring periodic velocity maps with 4D PCV-MRI measurements. Thus, more accurate comparisons between CFD simulation and experimental velocity maps in different groups of patients with upper airways disease should be possible.

REFERENCES

1. Sbirlea-Apiou, G., et al., *Simulation of the regional manifestation of asthma.* J Pharm Sci, 2004. **93**(5): p. 1205-16.
2. Martonen, T.B. and J.D. Schroeter, *Risk assessment dosimetry model for inhaled particulate matter: I. Human subjects.* Toxicol Lett, 2003. **138**(1-2): p. 119-32.
3. Kleinstreuer, C. and Z. Zhang, *Targeted drug aerosol deposition analysis for a four-generation lung airway model with hemispherical tumors.* J Biomech Eng, 2003. **125**(2): p. 197-206.
4. Oakes, J.M., et al., *Airflow and particle deposition simulations in health and emphysema: from in vivo to in silico animal experiments.* Ann Biomed Eng, 2014. **42**(4): p. 899-914.
5. Kimbell, J.S. and R.P. Subramaniam, *Use of computational fluid dynamics models for dosimetry of inhaled gases in the nasal passages.* Inhalation Toxicology, 2001. **13**(5): p. 325-334.
6. Lambert, A.R., et al., *Regional deposition of particles in an image-based airway model: large-eddy simulation and left-right lung ventilation asymmetry.* Aerosol Sci Technol, 2011. **45**(1): p. 11-25.
7. Corley, R.A., et al., *Comparative computational modeling of airflows and vapor dosimetry in the respiratory tracts of rat, monkey, and human.* Toxicol Sci, 2012. **128**(2): p. 500-16.
8. Tawhai, M.H. and C.L. Lin, *Airway gas flow.* Compr Physiol, 2011. **1**(3): p. 1135-57.
9. Kleinstreuer, C. and Z. Zhang, *Airflow and Particle Transport in the Human Respiratory System.* Annual Review of Fluid Mechanics, 2010. **42**: p. 301-334.
10. Johnstone, A., et al., *The flow inside an idealised form of the human extra-thoracic airway.* Experiments in Fluids, 2004. **37**(5): p. 673-689.
11. Tanaka, G., et al., *Spatial and temporal variation of secondary flow during oscillatory flow in model human central airways.* J Biomech Eng, 1999. **121**(6): p. 565-73.

12. Jedelsky, J., F. Lizal, and M. Jicha, *Characteristics of turbulent particle transport in human airways under steady and cyclic flows.* International Journal of Heat and Fluid Flow, 2012. **35**: p. 84-92.

13. Große, S., et al., *Time resolved analysis of steady and oscillating flow in the upper human airways.* Experiments in Fluids, 2007. **42**(6): p. 955-970.

14. Heenan, A.F., et al., *Experimental measurements and computational modeling of the flow field in an idealized human oropharynx.* Experiments in Fluids, 2003. **35**(1): p. 70-84.

15. Elkins, C.J. and M.T. Alley, *Magnetic resonance velocimetry: applications of magnetic resonance imaging in the measurement of fluid motion.* Experiments in Fluids, 2007. **43**(6): p. 823-858.

16. Anderson, J.R., et al., *Validation of computational fluid dynamics methods with anatomically exact, 3D printed MRI phantoms and 4D pcMRI.* Conf Proc IEEE Eng Med Biol Soc, 2014. **2014**: p. 6699-701.

17. Kung, E., et al., *In Vitro Validation of Patient-Specific Hemodynamic Simulations in Coronary Aneurysms Caused by Kawasaki Disease.* Cardiovasc Eng Technol, 2014. **5**(2): p. 189-201.

18. Biglino, G., et al., *Using 4D Cardiovascular Magnetic Resonance Imaging to Validate Computational Fluid Dynamics: A Case Study.* Front Pediatr, 2015. **3**: p. 107.

19. Isoda, H., et al., *Comparison of hemodynamics of intracranial aneurysms between MR fluid dynamics using 3D cine phase-contrast MRI and MR-based computational fluid dynamics.* Neuroradiology, 2010. **52**(10): p. 913-20.

20. Boussel, L., et al., *Phase-contrast magnetic resonance imaging measurements in intracranial aneurysms in vivo of flow patterns, velocity fields, and wall shear stress: comparison with computational fluid dynamics.* Magn Reson Med, 2009. **61**(2): p. 409-17.

21. Goubergrits, L., et al., *MRI-based computational fluid dynamics for diagnosis and treatment prediction: clinical validation study in patients with coarctation of aorta.* J Magn Reson Imaging, 2015. **41**(4): p. 909-16.

22. de Rochefort, L., et al., *Phase-contrast velocimetry with hyperpolarized 3He for in vitro and in vivo characterization of airflow.* Magn Reson Med, 2006. **55**(6): p. 1318-25.

23. Collier, G.J., et al., *Observation of cardiogenic flow oscillations in healthy subjects with hyperpolarized 3He MRI.* J Appl Physiol (1985), 2015. **119**(9): p. 1007-14.

24. Minard, K.R., et al., *MR imaging of apparent 3He gas transport in narrow pipes and rodent airways.* J Magn Reson, 2008. **194**(2): p. 182-91.

25. Minard, K.R., et al., *Phase-contrast MRI and CFD modeling of apparent (3)He gas flow in rat pulmonary airways.* J Magn Reson, 2012. **221**: p. 129-38.

26. Collier, G.J. and J.M. Wild, *In vivo measurement of gas flow in human airways with hyperpolarized gas MRI and compressed sensing.* Magn Reson Med, 2015. **73**(6): p. 2255-61.

27. de Rochefort, L., et al., *In vitro validation of computational fluid dynamic simulation in human proximal airways with hyperpolarized 3He magnetic resonance phase-contrast velocimetry.* J Appl Physiol (1985), 2007. **102**(5): p. 2012-23.

28. Minard, K.R., et al., *Application of magnetic resonance (MR) imaging for the development and validation of computational fluid dynamic (CFD) models of the rat respiratory system.* Inhal Toxicol, 2006. **18**(10): p. 787-94.

29. Newling, B., et al., *Velocity imaging of highly turbulent gas flow.* Phys Rev Lett, 2004. **93**(15): p. 154503.

30. Jalal, S., et al., *Three-dimensional inspiratory flow in a double bifurcation airway model.* Experiments in Fluids, 2016. **57**(9).

31. Banko, A.J., et al., *Three-dimensional inspiratory flow in the upper and central human airways.* Experiments in Fluids, 2015. **56**(6).

32. Bernate, J.A., et al., *Study of the flow unsteadiness in the human airway using large eddy simulation.* Physical Review Fluids, 2017. **2**(8).

33. Banko, A.J., et al., *Oscillatory flow in the human airways from the mouth through several bronchial generations.* International Journal of Heat and Fluid Flow, 2016. **61**: p. 45-57.

34. Giesel, F.L., et al., *Rapid prototyping raw models on the basis of high resolution computed tomography lung data for respiratory flow dynamics.* Acad Radiol, 2009. **16**(4): p. 495-8.

35. Collier, G., et al., *Velocity mapping of gasflow in the upper airways of a lung model for validation of computational fluid dynamics simulations.* In Proceedings of the 21st annual Meeting of ISMRM, Salt Lake City, Utah, USA, 2013. Abstract 1458.

36. Nicoud, F. and F. Ducros, *Subgrid-scale stress modelling based on the square of the velocity gradient tensor.* Flow Turbulence and Combustion, 1999. **62**(3): p. 183-200.

37. Ayachit, U., *The ParaView Guide: A Parallel Visualization Application*. 2015: Kitware, Inc. 276.

38. Tsuda, A., F.S. Henry, and J.P. Butler, *Particle transport and deposition: basic physics of particle kinetics.* Compr Physiol, 2013. **3**(4): p. 1437-71.

39. Lin, C.L., et al., *Characteristics of the turbulent laryngeal jet and its effect on airflow in the human intra-thoracic airways.* Respir Physiol Neurobiol, 2007. **157**(2-3): p. 295-309.

Table 1
Sequence parameters used for 3D-PCV MRI protocol. Q: experimental flow rate, Tacq: acquisition time, SENSE AF: acceleration factor for parallel imaging in the superior inferior direction. Model 1: central airway tree only, model 2: central airway tree + upper airways.

Model	Q (mL/s)	Venc (cm/s)	FOV (mm^3)	T_E/T_R (ms)	Tacq (min)	Original matrix size	DICOM resolution (mm^3)	SENSE AF
1	3.7	5	270 x 179 x 350	7.1/13.2	14	270 x 179 x 175	0.53 x 0.53 x 1	2
1	8	10	270 x 179 x 350	5.8/9.6	10	270 x 179 x 175	0.53 x 0.53 x 1	2
2	3.5	10	200 x 160 x 300	5.0/9.3	15	200 x 160 x 150	0.39 x 0.39 x 1	1
2	3.5	30	200 x 160 x 300	3.5/7.3	12	200 x 160 x 150	0.39 x 0.39 x 1	1

Table 2
Regression results from pixel by pixel comparison of velocity components between the 3D PCV-MRI measurements and CFD simulations. All results are presented with standad error.

Airway model	Central airway tree only						Including upper airways and oral cavity		
Q (mL/s)	3.7			8			3.5		
Velocity component	V_x	V_y	V_z	V_x	V_y	V_z	V_x	V_y	V_z
y-intercept (cm/s)	0.0279 ± 0.0002	0.0523 ± 0.0002	0.0070 ± 0.0004	0.0435 ± 0.0004	0.0964 ± 0.0004	0.103 ± 0.001	-0.118 ± 0.002	0.673 ± 0.004	0.493 ± 0.004
slope	0.815 ± 0.001	0.9171 ± 0.0005	1.0046 ± 0.0004	0.890 ± 0.001	0.9349 ± 0.0005	1.0307 ± 0.0006	0.631 ± 0.001	0.549 ± 0.002	0.784 ± 0.001
R^2	0.65	0.92	0.94	0.68	0.91	0.9	0.59	0.39	0.73

Figure captions:

Figure 1: Solid 3D printed models of the two patient-specific lung central airways used for the study. **a)**: first model, central airways only, **b)**: workflow for the creation of the second model including the upper airways and oral cavity derived from the segmentation of MRI images.

Figure 2: Comparison between CFD simulations and PCV-MRI measurements in the lung model of the central airways. **a)** & **b)**: 3D visualization of the flow patterns measured by PCV-MRI and predicted by CFD simulations respectively (water flow of 3.7 mL/s). The colormap represents the velocity magnitude in cm/s. **c)**, **d)** & **e)**: pixel by pixel comparison and linear regression line of the velocity values along the x, y and z directions respectively from the data sets displayed in **a)** and **b)** (see axes orientation at the top right corner). **f)**: comparison of the flow values derived from the CFD and MRI data sets at different slice locations (squares: trachea, circles: main bronchi, left lower lobe bronchus and truncus intermedius, triangles: lobes and crosses: segments) for the combined experimental water flows of 3.7 and 8 mL/s (solid line: identity line).

Figure 3: Comparison between CFD simulations and PCV-MRI measurements in the lung model of the central and upper airways for a water flow of 3.5 mL/s. **a)** & **b)**: 3D visualization of the flow patterns measured by PCV-MRI and predicted by CFD simulations respectively. The colormap represents the velocity magnitude in cm/s and uses logarithmic scale. **c)**: pixel by pixel comparison and linear regression line of the velocity values along the z direction (see axes orientation at the bottom of a)). **d)**: Comparison of the flow values derived from the CFD and MRI data sets at different slice locations (squares: trachea, circles: main bronchi, left lower lobe bronchus and truncus intermedius, triangles: lobes).

Figure 4: Comparison between CFD simulations and 2D/1D PCV-MRI measurements in the lung model of the central and upper airways. **f)**: Schematic representation of the positions of the cross sections. **a)** to **e)**: 2D (top)/1D (bottom) velocity profiles comparison between CFD simulations (right) and PCV-MRI measurement (left) for cross sections S1 to S5 respectively at Q = 20 mL/s. The colormaps of the 2D velocity profiles are in cm/s. The semi-transparent black lines of each plot represent the successive velocity profiles (time resolution of 30 ms), the red solid line is the average velocity profile ± SD (red dashed solid lines). **g)**: mean standard deviation of the velocity profiles for the different cross sections S1 to S5 at Q = 20 mL/s. **f)**: mean standard deviation of the velocity profile normalized by the average velocity at cross section S4 for different experimental flows (Q = 4.5, 6, 13, 27 mL/s).